The Astrophysical Journal, 585:1062–1072, 2003 March 10

ELEMENTAL ABUNDANCES FOR THE 1996 STREAMER BELT

M. Uzzo,[1] Y.-K. Ko,[1] J. C. Raymond,[1] P. Wurz,[2] and F. M. Ipavich[3]

Received 2002 October 21; accepted 2002 November 14

ABSTRACT

The purpose of this paper is to explore the observed physical characteristics of the solar corona streamer belt from 1996 June 1 to August 5. The UV spectral data was collected by the Ultraviolet Coronagraph Spectrometer (UVCS) instrument on board the *Solar and Heliospheric Observatory* (*SOHO*) spacecraft. From this data the abundances of oxygen, silicon, and magnesium were determined on an almost daily basis during this time period at both the west and east limbs. The streamer belt was composed of both active and quiescent streamers, which allows for the comparison of these two categories of magnetic field structures. The depletion of these three elemental abundances in the core of quiescent streamers was found, as in previous observations. The variance in abundance with solar rotation was investigated as a consequence of the long time frame considered here. The first ionization potential (FIP) effect was present in the data, and the danger of exploring this phenomena by the traditional FIP bias was also covered. A comparison with in situ elemental abundance data from the Charge, Element, and Isotope Analysis System (CELIAS) instrument on *SOHO* provides evidence suggesting that active-region streamers and the outer "leg" structural component of quiescent streamers are definite contributors to the slow solar wind.

Subject headings: solar wind — Sun: abundances — Sun: corona

1. INTRODUCTION

The most common method for studying the corona has been to observe the visible light produced by the electron-scattered continuum of the K corona. The dominant white-light feature of the corona during solar minimum is a continuous streamer belt located near the equatorial plane of the Sun. The streamer belt is a region of high coronal density lying above the equatorial magnetic neutral line. Tangencies of the sheet of dense gas to the line of sight appear bright in coronagraph images (e.g., Wang et al. 1997). The streamer as defined by a high observed density probably includes two parts: a closed field region corresponding to the center of the streamer, or streamer "core," and the neighboring open field lines, sometimes called the "legs" of the streamer. Because the outflow speed along the legs is subsonic, below $\sim 3\ R_{\odot}$ (e.g., Strachan et al. 2002), the density structure is nearly hydrostatic, and the density is similar to that in the streamer core. However, the core and legs can sometimes be distinguished by differences in the elemental abundances (Raymond et al. 1997). The region referred to here as a streamer leg is sometimes called the coronal hole boundary (e.g., Wang et al. 1991).

A neutral point exists at the apex of the closed field lines, forming the cusp in the helmet structure, and above this a current sheet extends out into the heliosphere. The streamer stalk, which starts at the cusp and continues outward, is composed of open field lines on either side of the current sheet. The slow solar wind may arise from the streamers in several ways. LASCO (Large Angle and Spectrometric Coronograph Experiment) movies show blobs detaching from the streamer cusp and accelerating to the slow solar wind speed (Sheeley et al. 1997; Wang et al. 2000). These blobs result from reconnection between open and closed fields (e.g., Wang et al. 1998, 2000), from expansion and pinching off of closed loops (e.g., Suess et al. 1999), or from plasmoid formation by reconnection (e.g., Linker & Mikić 1995). Both white-light estimates (Wang et al. 1998, 2000) and differences between the elemental abundances in the closed field region (Raymond et al. 1997) indicate that these blobs constitute a small fraction of the slow wind.

The bulk of the slow wind arises from the streamer legs, and there are several suggestions for its nature. Wang & Sheeley (1991) argue that the slow wind is driven in the same manner as the fast wind but that a larger area spreading factor in the coronal hole boundary leads to the slow wind solution. Vásquez (2002) finds that the magnetic structure near the cusp leads to a critical point above the cusp and a consequent slow-wind solution. Suess et al. (1999a) obtain slow wind in the streamer legs by assuming that heat is deposited more efficiently in electrons than in protons near the equator. Fisk & Schwandon (2001) computed the diffusion of open field lines by reconnection between open and closed fields, and in their model the slow wind arises where this process opens previously closed loops at the coronal hole–streamer boundary.

Streamers can be broken down into two categories, quiescent and active-region streamers. Quiescent streamers are stable long-lived structures that have an interesting UV signature. Raymond et al. (1997) found that for quiescent-streamer structures the intensities from heavy ions such as O VI features a dimmer core relative to the edges. In that paper the O VI bright streamer edges were referred to as legs and the dimmer central region was referred to as the core. The same terms are adopted for this paper. Active-region streamers are more dynamic than their quieter quiescent cousins and typically lack their unusual UV signature. Their lack of a depleted core could result from projection effects or the cusp located below the observation height. These streamers may be composed of several open and closed magnetic field structures continually interacting with each other.

[1] Harvard-Smithsonian Center for Astrophysics, 60 Garden Street, Cambridge, MA 02138.
[2] Physikalisches Institut der Universitat Bern, CH-3012 Bern, Switzerland.
[3] University of Maryland, College Park, MD 20742.

The next section provides some information about the Ultraviolet Coronagraph Spectrometer (UVCS) instrument and the observational program, which produced the UV data analyzed here. In § 3 the streamer morphology in terms of ultraviolet intensities and outflow velocities is explored. Utilizing this information the rationale for how the active region and quiescent streamers were sampled is explained. This is followed by § 4, which goes through the abundance calculations. Section 5 introduces the results, with specific aspects of said results explored in the following subsections. This includes the abundance spatial structure for quiescent streamers (§ 5.1), the manifestation of the first ionization potential (FIP) effect (§ 5.2) and how the abundances for both active and quiescent streamers vary with solar rotation (§ 5.3). In § 5.4 a comparison to the streamer abundances calculated by Raymond et al. (1997) and Ko et al. (2002) is conducted. Then § 6 covers the Charge, Element, and Isotope Analysis System (CELIAS) instrument and the abundance results are compared to those derived from remote sensing. The final section summarizes the conclusions from this research. Almost all of the data presented here were produced by instruments on board the *Solar and Heliospheric Observatory* (*SOHO*). The solar disk images were produced by the Extreme-Ultraviolet Imaging Telescope (EIT) (Delaboudinière et al. 1995). The in situ data were collected by CELIAS (Hovestadt et al. 1995) Mass Time of Flight (MTOF), Charge Time of Flight (CTOF), and Proton Monitor (PM) experiments. The spectral data of the corona were produced by UVCS (Kohl et al. 1995).

2. OBSERVATIONS

The UVCS instrument conducts ultraviolet observations of the corona from a heliocentric distance of 1.5–10 solar radii ($R_\odot$). The instantaneous field of view (FOV) for UVCS is a 42′ slice of the corona parallel to the tangent of the solar limb. The radial dimension of the FOV corresponds to the slit width for the spectrometer. This FOV can be rotated nearly 360° around the Sun-centered point. Radiation from the solar disk is rejected by a fixed external occulter and an adjustable internal occulter. The internal occulter cuts down the stray light by adjusting the amount of exposed mirror. The mirror angle selects the observation height. The reflected radiation enters the spectrometer housing through an adjustable slit. It then strikes the spectrometer's grating (UV channels), and the resulting diffracted spectrum is recorded by the detector assembly.

The UVCS instrument possesses three channels, one visible and two ultraviolet. However, only data from the ultraviolet channel designed for optimal observations of the O VI ($\lambda\lambda$1032, 1037) doublet are used here. The wavelength range for this channel, 945–1123 Å (473–561 Å in second order), was obtained by altering the grating angle to the incident radiation. This channel has an additional redundant mirror designed to reflect the Lyα (1215 Å) line onto the O VI detector. This extends the wavelength range from 1160 to 1270 Å (580–635 Å in second order). Because of data transmission restrictions, the full-resolution spatial and spectral ranges observed by the O VI channel detector could not be transmitted from the *SOHO* spacecraft. A balance between the ranges of the spatial and spectral components, as well as the binning thereof, was required. This is accomplished by a detector mask that selects particular portions of the detector and bins the data. For a complete description of the UVCS instrument we refer to Kohl et al. (1995).

A synoptic program has been conducted nearly every day since UVCS started collecting data in 1996. During the period of the mission considered here the synoptic programs lasted for 14 hr a day and provided complete 360° coverage of the corona. This was done by observing at eight fixed roll angles. At each angle several heights were sampled in order to derive a record of the daily changes occurring in the corona. The data reported here come from observations conducted from 1996 June 1 to August 5. The white-light corona image of Figure 1, produced by the Mark-III K coronameter from the Mauna Loa Solar Observatory in Hawaii, shows the structure on 1996 June 26. Since the streamer structures were confined to a belt, which roughly coincided with the equatorial plane as displayed in this image, only the west- and east-limb observations are considered here.

In Figure 1 the UVCS FOV was superposed onto the image to depict the approximate location of the 1.7 $R_\odot$ west-limb observation. Although the UVCS synoptic program observes at multiple heights at the east and west limbs, the observation at 1.7 $R_\odot$ possessed the highest count rates and exposure times to make the abundance calculations statistically meaningful. Included within the UVCS FOV representation are the O VI 1032 Å (*left*) and Lyα (*right*) spatial profiles recorded for that day. The total exposure time at this height was approximately 1500 s for each day and limb. From these synoptic observations it was possible to determine the absolute abundances of oxygen, silicon, and magnesium. The 38′ mask allowed the study of how these abundances vary with latitude. As a consequence of the 2 months of nearly continuous synoptic observations, the morphologies of these three abundances were mapped out. This illustrated how the streamer belt varied with time and longitude combined.

3. STREAMER MORPHOLOGY

The spatial (latitudinal) morphology of streamers can vary depending on the wavelengths being examined, the type of streamer that is observed, and projection effects. Figures 2 and 3 are composite images created from UVCS data depicting the corona at 1032 Å (O VI) and 1215 Å (Lyα), respectively. The inner components of Figures 2 and 3 are EIT images of the solar disk in 284 Å (Fe XV) and 195 Å (Fe XII), respectively. The solar disk in both wavelengths shows several active regions between the east limb and the disk center. However the west limb shows a distinct lack of active regions. By comparing the west limbs in both images one can see that the individual streamer in Lyα appears as a double streamer structure in O VI or as a single streamer with a darker core. This phenomenon is also illustrated in the UVCS spatial profiles of Figure 1. This O VI spatial signature will henceforth define our definition of a quiescent streamer. The east-limb streamer, located above several active regions and therefore designated an active-region streamer, does not possess this same O VI signature.

The drop in O VI doublet intensity at the core of quiescent streamers is not caused by a projection effect. If this were the case, a similar drop in the Lyman series (Lyα 1215 Å and Lyβ 1025 Å) of hydrogen would have also been recorded. The spatial profiles found in Figure 4 for 1996 June 26 at the west limb illustrate the two very different

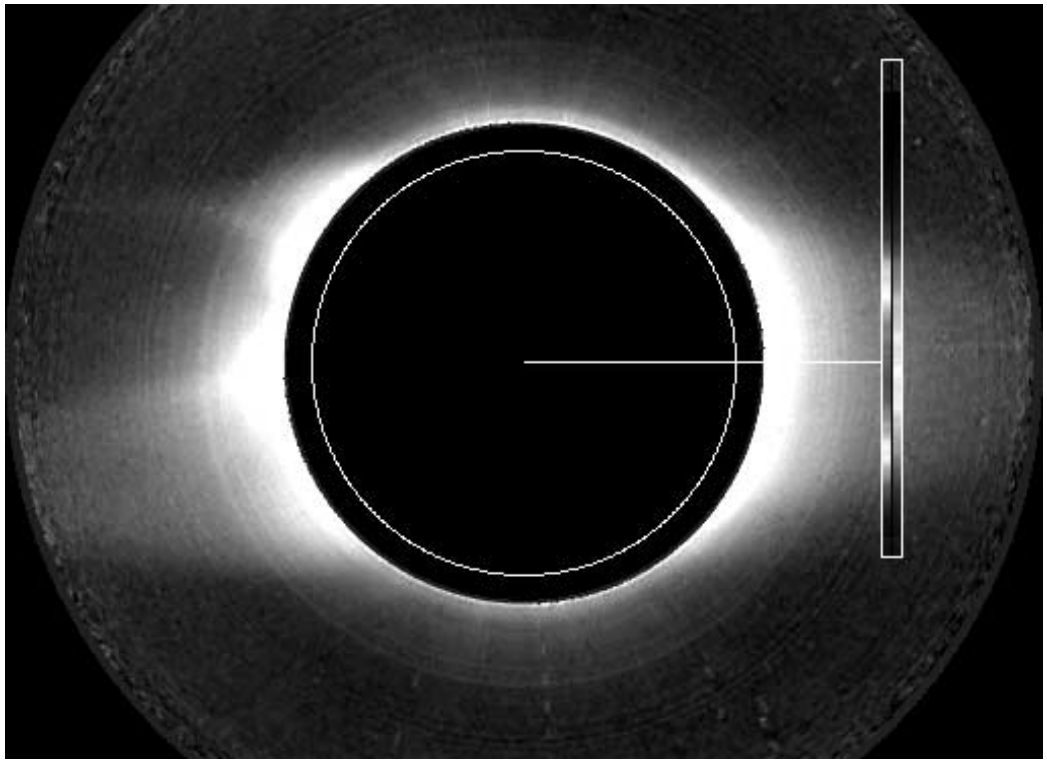

FIG. 1.— Visible light image of 1996 June 26 from the Mauna Loa Solar Observatory MK3 Coronameter. The UVCS FOV is superposed on the image at the approximate location of the west-limb observation at 1.7 $R_{\odot}$. The resulting UVCS observations of O VI 1032 Å (*inner strip*) and Lyα 1215 Å (*outer strip*) for the same day are included within the FOV box.

intensity structures being discussed. The intensity of the O VI 1032 Å line was increased by a factor of 40 in order to scale it to the brighter Lyα line. As will be covered below, the discrepancy between intensity morphologies of the O VI doublet and the Lyman series indicates a depletion in the oxygen abundance in the cores of quiescent streamers (Raymond et al. 1997). The observations presented here also indicated a similar depletion in the silicon and magnesium abundances as well. The profiles provided in Figure 5 are the east-limb intensities for the same day. They show an O VI spatial signature that was similar to that of Lyα, compared in Figure 4. For both Figures 4 and 5, the direction of solar north is indicated. The oxygen intensity signature identified as a quiescent streamer has been investigated in several previous publications (e.g., Raymond et al. 1997, 1998; Marocchi, Antonucci, & Giordano 2001). While several other possible explanations for this difference between the Lyman series and other line intensity profiles have been explored, for example, Noci et al. (1997), the abundance argument seems to be the strongest.

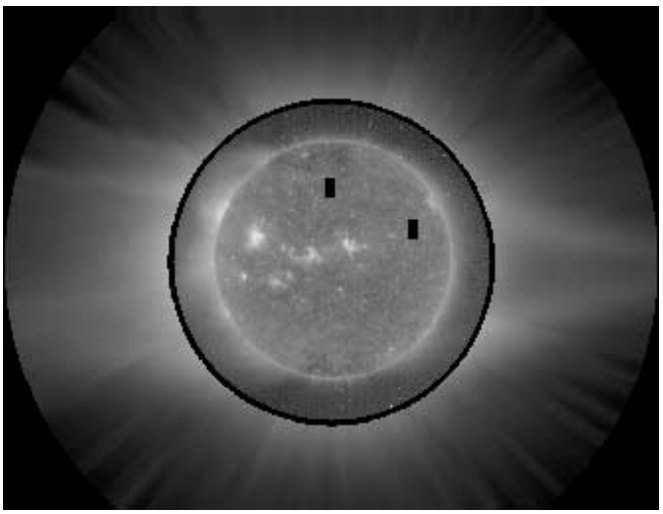

FIG. 2.—Composite image of the low corona (EIT Fe XV 284 Å line) and the outer corona (UVCS O VI 1032 Å line composite) from 1996 June 26.

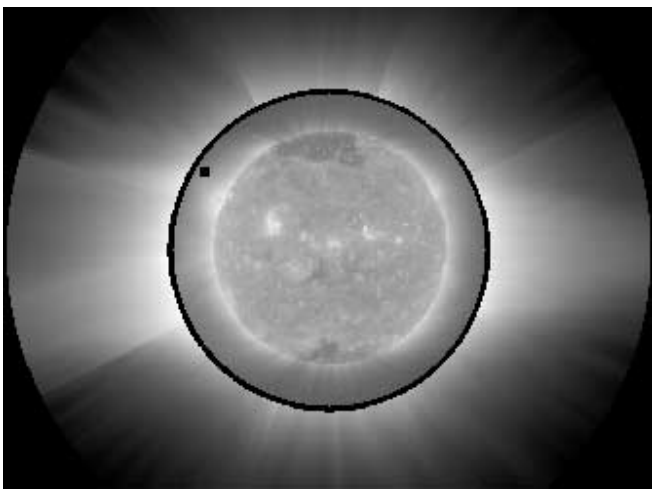

FIG. 3.—Composite image of the low corona (EIT Fe XII 195 Å line) and the outer corona (UVCS Lyα 1215 Å line composite) from 1996 June 26.

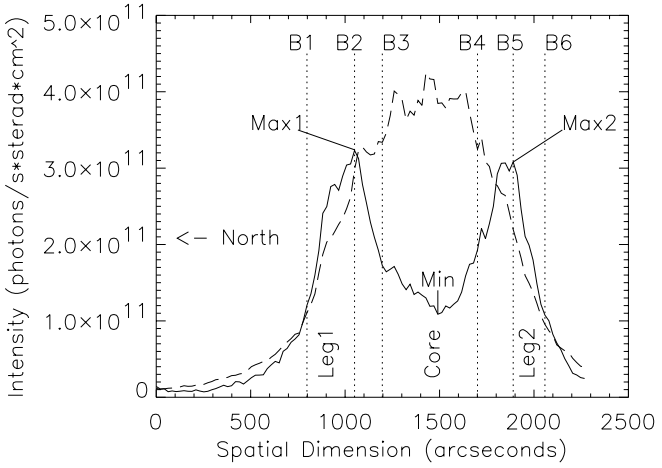

FIG. 4.—Quiescent streamer spatial boundary derivation from the west-limb observation at 1.7 $R_\odot$ for 1996 June 26. The spatial morphologies are Lyα (*dashed line*) and O VI (*solid line*) intensities, where the O VI signal was scaled by a factor of 40. The three zones of the quiescent streamer are defined by the six boundaries, B1 through B6, represented by the vertical dotted lines.

The results from a study on outflow velocities of quiescent streamers were recently published by Strachan et al. (2002). The authors found that in the cores of quiescent streamers the outflow velocity was essentially zero. The outflow velocity increases sharply near the O VI intensity peaks and continues along the outer edges of the streamer. This has been attributed to the transition from the closed magnetic field lines within the center of the streamer to the surrounding open field lines. Strachan et al. (2002) reported that based on velocity measurements the outer edges of the quiescent streamer legs, which become the streamer stalks above the cusp, are sources of material for the slow solar wind. Raymond et al. (1997) came to the same conclusion concerning the streamer—slow solar wind connection based on an abundance analysis. These results agree with the conclusions by Woo & Martin (1997) and Habbal et al. (1997), who also determined that streamer stalks are a slow solar wind source region. It was the determination of the O VI intensity peaks as the boundary between essentially zero and nonzero outflow velocity regions that led to the decision to choose these maxima as the inner boundaries of the quiescent leg structures, as discussed below.

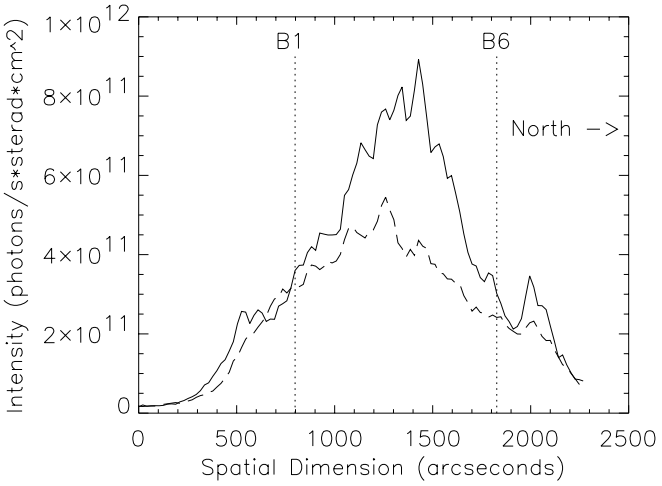

FIG. 5.—Active-region streamer spatial boundary derivation from the east-limb observation at 1.7 $R_\odot$ for 1996 June 26. The spatial morphologies are Lyα (*dashed line*) and O VI (*solid line*) intensities, where the O VI signal was scaled by a factor of 40. The one zone required for an active-region streamer is defined by the boundaries B1 and B6, represented by the vertical dotted lines.

For the quiescent streamer observations a three-zone sampling was applied in order to investigate the distinctive core and leg structures. Figure 4 graphically illustrates the boundaries selected for this specific day as an example. The determination of the boundaries, B1 through B6, is based entirely on the O VI 1032 Å spatial profile. The maximum intensities for the first and second legs are designated Max1 and Max2, respectively. The minimum intensities located between the locations of Max1 and Max2 is referred to as Min. From the velocity analysis of quiescent streamers mentioned above (Strachan et al. 2002), the logical position for the inner boundaries of the leg structures was at Max1 for B2 and Max2 for B5. The first and last boundaries, B1 and B6, are located at the spatial position where the intensities of Max1 and Max2 have dropped by a factor of $1/e$, respectively. Marocchi et al. (2001) used the same criteria for defining their streamer boundaries. For active-region streamers (see the example in Fig. 5) the boundaries B1 and B6 are determined the same way as for the quiescent case, except with only one maximum defined. The boundaries B3 and B4 for the core sampling are located at the positions where the intensities are near those given by equation (1). With the exception of B2 and B5, the boundaries selected here were a compromise between isolating the individual structures and maintaining a high enough number of counts to make the sampling statistically meaningful:

$$I_{B3} = \mathrm{Min} + (\mathrm{Max1} - \mathrm{Min})e^{-1}\,,$$
$$I_{B4} = \mathrm{Min} + (\mathrm{Max2} - \mathrm{Min})e^{-1}\,. \quad (1)$$

4. ABUNDANCE CALCULATIONS

Since the chosen grating positions and masks used for the synoptic contain both Lyα and Lyβ, the absolute elemental abundance (the abundance of an element relative to hydrogen) could be derived for oxygen, silicon, and magnesium. Examining the photospheric normalized absolute abundances proved to be a great asset and allows for the FIP effect to be explored from a different perspective. In many observations the abundance of a low-FIP element, such as magnesium, was determined relative to the abundance of a high-FIP element, e.g., oxygen or neon. In order to derive the silicon and magnesium abundances, the spectral lines Si XII 499 Å and Mg 609 Å are used. The Lyβ line is located near both the O VI doublet (1032 and 1037 Å) and the Si XII 499 Å lines on the detector in the primary light path of the O VI channel. The Lyα and Mg X 609 Å are obtained through the redundant path. In order to minimize the instrumental uncertainty for the oxygen calculations, which is the abundance we are most interested in, the collisional component of the Lyβ line provided the data for determining the hydrogen contribution to the abundance ratio instead of Lyα.

The first step in calculating the abundances is to separate the collisional and radiative components of the spectral lines. Only the Lyman series and the O VI doublet posses

any significant radiative contributions in their signals (Raymond et al. 1997). From the ratio of the O VI doublet, 1032/1037 Å, the two components can be separated by utilizing the fact that the collisional contribution is 2 : 1 while the radiative is 4 : 1. For the Lyman series the collisional and radiative contributions are not as clear. By assuming an electron temperature of $\log_{10}(T_e) = 6.2$ for the streamer plasma and the disk intensities, both provided by Raymond et al. (1997), we can employ their values for the radiative (13,020 : 14.3) and collisional (21.8 : 2.88) component ratios of Lyα over Lyβ.

While it is possible to calculate the oxygen abundances from both the collisional and the radiative components of the O VI radiation, only the former will be presented at this time. A discrepancy between the collisional and radiative derived results has been known and discussed in previous publications (e.g., Raymond et al. 1997; Parenti et al. 2000; and Marocchi et al. 2001). The same discrepancy was also found for this data, and no new insights were discovered concerning a possible explanation. Therefore, this subject will be deferred to a later paper, and the radiative results will not be presented here.

The abundances for oxygen, silicon, and magnesium are calculated from equation (2) (Raymond et al. 1997). The term $(N_O/N_H)/(N_O/N_H)_{ph}$ is the absolute abundance that is normalized by its photospheric value, $(N_O/N_H)_{ph} = 6.607 \times 10^{-4}$ (Allen 1973). The measured collisional intensity and the collisional excitation rate are I_{coll} and q, respectively. The branching ratio is represented by B, and the ion fraction, which is dependent on the electron temperature, by C. The values for the parameters are obtained by substituting the CHIANTI emissivities, ε (Dere et al. 1997, 2001), which reduces equations (2) and (3) (for a more detailed coverage of the abundance equation terms the reader is directed to Raymond et al. [1997 and references therein]):

$$\frac{N_O/N_H}{(N_O/N_H)_{ph}} = \frac{I_{coll}(1032)}{I_{coll}(\mathrm{Ly}\beta)} \frac{C_{H\,I}}{C_{O\,VI}} \frac{B_{Ly\beta}}{B_{O\,VI}} \frac{q_{Ly\beta}}{q_{1032}} \frac{N_{Hph}}{N_{Oph}} , \quad (2)$$

$$\frac{N_O/N_H}{(N_O/N_H)_{ph}} = \frac{I_{coll}(1032)}{I_{coll}(\mathrm{Ly}\beta)} \frac{\varepsilon(\mathrm{Ly}\beta)}{\varepsilon(\mathrm{O\,VI})} . \quad (3)$$

5. ABUNDANCES RESULTS

The abundance results, Figures 6–11, are given as the photospheric normalized absolute abundance versus the day of year (DOY). The asterisks represent observations where a one-zone sampling was used for those streamers identified as an active-region streamer. When an entry has three open diamonds, this means the streamer was categorized as a quiescent streamer. In those cases the solid lines represent the first leg, which is to the south of the core for east-limb observations and to the north for the west limb. The dashed lines represent the second leg, and the dotted lines are the abundances derived from the core. The abundance results for oxygen are provided in Figures 6 and 7 for the west and east limbs, respectively. The magnesium abundances are shown in Figure 8 (west) and Figure 9 (east), while the results for silicon are shown in Figure 10 (west) and Figure 11 (east). The shaded regions of these six plots illustrate the CELIAS MTOF in situ abundance results, which will be discussed in § 6.

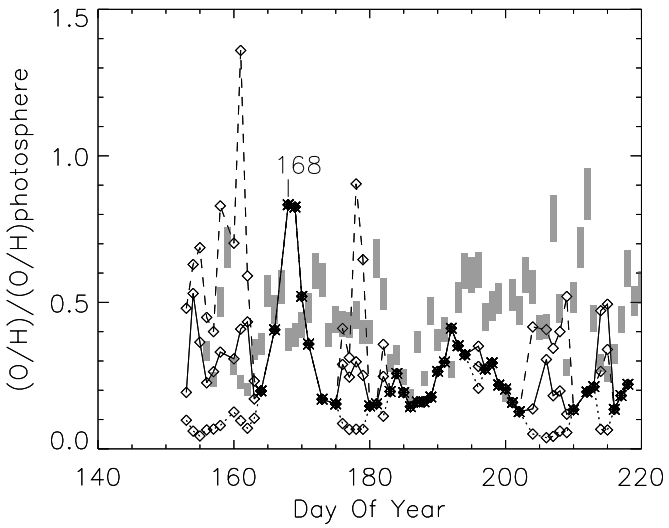

FIG. 6.—Oxygen absolute elemental abundances derived from west-limb observations from 1996 June 1 to August 5. Corresponding CELIAS in situ results with error range are depicted as shaded area. CELIAS data adjusted by ≈+3 days to compensate for solar rotation and slow solar wind time of flight to 1 AU. The asterisks represent active-region streamers (one zone), and the sets of three open diamonds identify quiescent-streamer components (*solid line:* first leg; *dashed line:* second leg; *dotted line:* core).

The sources of error for the data provided in Figures 6–11 will be outlined in general. For a more detailed coverage of the instrument characteristic, the reader is directed to Kohl et al. (1995), Pernechele et al. (1995), and Gardner et al. (1996). The external and internal occulters cut down the stray light to a degree that its contribution becomes negligible for observations of streamers. The data were calibrated using standard techniques that have a radiometric uncertainty of approximately 20% for the O VI doublet and Lyman series lines (first-order lines). For the silicon and magnesium lines the systematic error can be upward of 50% (second-order lines; Gardner et al. 2000, 2003).

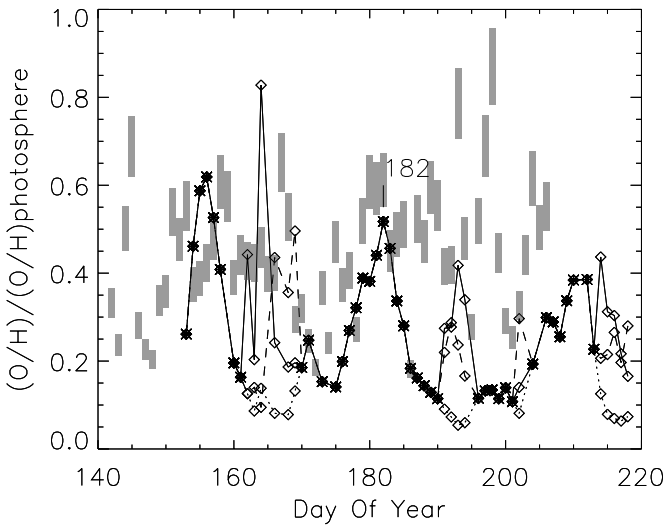

FIG. 7.—Oxygen absolute elemental abundances derived from east-limb observations from 1996 June 1 to August 5. Corresponding CELIAS in situ results with error range are depicted as shaded area. CELIAS data adjusted by ≈−11 days to compensate for solar rotation and slow solar wind time of flight to 1 AU. See Fig. 6 for symbol identifications.

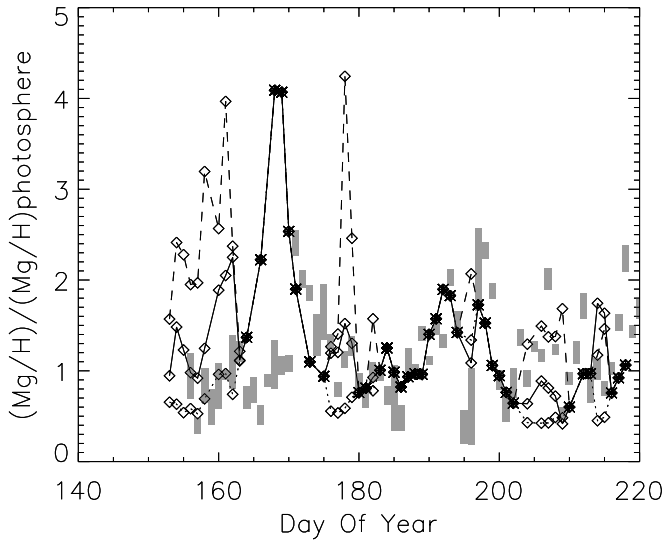

FIG. 8.—Magnesium absolute elemental abundances derived from west-limb observations from 1996 June 1 to August 5. Corresponding CELIAS in situ results with error range are depicted as shaded area. CELIAS data adjusted by ≈+3 days to compensate for solar rotation and slow solar wind time of flight to 1 AU. See Fig. 6 for symbol identifications.

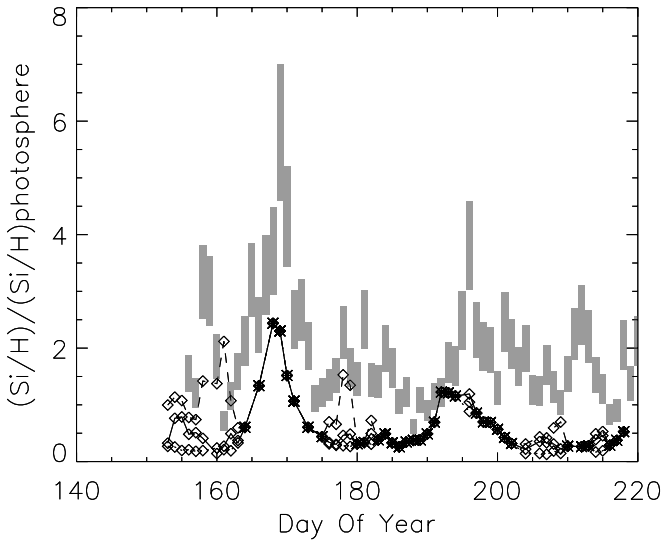

FIG. 10.—Silicon absolute elemental abundances derived from west-limb observations from 1996 June 1 to August 5. Corresponding CELIAS in situ results with error range are depicted as shaded area. CELIAS data adjusted by ≈+3 days to compensate for solar rotation and slow solar wind time of flight to 1 AU. See Fig. 6 for symbol identifications.

Error bars are omitted from the graphed data points since they would obscure the data, especially for the quiescent streamers, which are defined by three samplings per DOY entry. The statistical errors range from 10% to 75%, depending on the coronal structure and spectral line under consideration. As mentioned earlier, the data were collected from the synoptic observation program and not from a dedicated abundance study. Therefore the statistics are lower than preferred, which limits us to drawing general conclusions based on the trends in the data. Even so, several significant insights have been drawn from this data.

5.1. *Quiescent Streamers*

The quiescent streamer observation sets are DOY 153–163, 176–179, and 204–209 for the west limb, while for the east limb they are 162–169, 191–194, and 214–218. The time- and structure-averaged results for the west and east limbs are provided in Tables 1 and 2, respectively. The abbreviations in the tables are active-region (AR) streamer, quiescent-streamer core (QC), and quiescent-streamer leg 1 (QL1) or leg 2 (QL2). The standard deviations for the three elemental abundances are also provided. For nearly all of the quiescent observation sets, the core structures displayed a significant depletion in oxygen, silicon, and magnesium

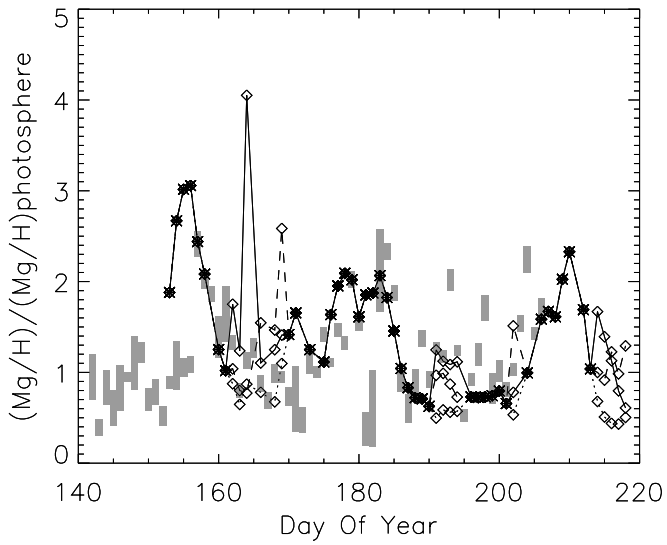

FIG. 9.—Magnesium absolute elemental abundances derived from east-limb observations from 1996 June 1 to August 5. Corresponding CELIAS in situ results with error range are depicted as shaded area. CELIAS data adjusted by ≈−11 days to compensate for solar rotation and slow solar wind time of flight to 1 AU. See Fig. 6 for symbol identifications.

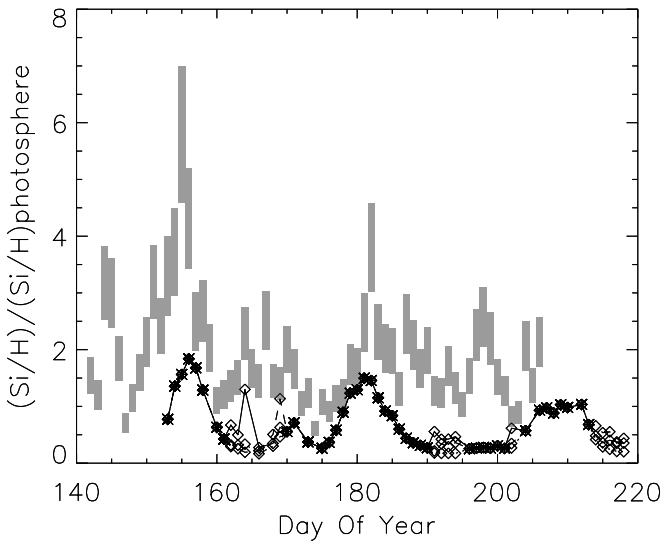

FIG. 11.—Silicon absolute elemental abundances derived from east-limb observations from 1996 June 1 to August 5. Corresponding CELIAS in situ results with error range are depicted as shaded area. CELIAS data adjusted by ≈−11 days to compensate for solar rotation and slow solar wind time of flight to 1 AU. See Fig. 6 for symbol identifications.

TABLE 1
West Limb Absolute Abundance Results

		Abundances			FIP Bias	
DOY Range	Type	$[O/H]/[O/H]_{ph}$	$[Si/H]/[Si/H]_{ph}$	$[Mg/H]/[Mg/H]_{ph}$	$[Si/O]/[Si/O]_{ph}$	$[Mg/O]/[Mg/O]_{ph}$
153–162.....	QL1	0.340 ± 0.101	0.465 ± 0.200	1.443 ± 0.476	1.370	4.251
153–162.....	QL2	0.681 ± 0.272	1.191 ± 0.392	2.476 ± 0.680	1.749	3.638
153–162.....	QC	0.079 ± 0.023	0.217 ± 0.029	0.700 ± 0.156	2.760	8.904
166–171.....	AR	0.589 ± 0.203	1.732 ± 0.542	2.963 ± 0.933	2.942	5.034
176–179.....	QL1	0.270 ± 0.023	0.398 ± 0.077	1.305 ± 0.131	1.471	4.827
176–179.....	QL2	0.568 ± 0.229	1.058 ± 0.385	2.344 ± 1.190	1.863	4.125
176–179.....	QC	0.072 ± 0.008	0.287 ± 0.017	0.597 ± 0.067	3.998	8.322
190–198.....	AR	0.311 ± 0.046	0.921 ± 0.260	1.609 ± 0.174	2.959	5.167
204–209.....	QL1	0.188 ± 0.065	0.287 ± 0.056	0.694 ± 0.163	1.531	3.698
204–209.....	QL2	0.417 ± 0.057	0.491 ± 0.137	1.444 ± 0.136	1.177	3.461
204–209.....	QC	0.050 ± 0.008	0.149 ± 0.019	0.450 ± 0.029	3.001	9.055

relative to their leg structures. The leg abundance results were found to fluctuate by as much as a factor of 4, which may be primarily due to the low Lyβ intensities found in these structures (see eq. [3]), although projection effects cannot be ruled out. The one data point in Figure 6 that indicates an oxygen enhancement on DOY 161 is most likely an example of this condition.

One possible explanation for the observed depletion in the core of quiescent streamers is gravitational settling (Raymond et al. 1997, 1998). The quiescent streamer is stable over a period of weeks to months. The plasma that travels along these field lines already has the FIP abundance pattern, which is believed to be set in the chromosphere. The FIP effect and its manifestation in the UVCS data will be discussed in § 5.3. The material located in the streamer core is trapped, and within a few days these three elements, relative to hydrogen, will settle back toward the photosphere as a result of the effects of gravity. The material located along the outer magnetic field lines of the streamer, however, escapes into the heliosphere and thereby contributes to the slow solar wind (see § 6). This concept is supported by the findings of Ofman et al. (2000) and Strachan et al. (2002). An alternative picture invokes reconnection between open field lines and closed loops, with the FIP enhancement occurring while the plasma is trapped in the closed loops (e.g., Schwadron, Fisk, & Zurbuchen 1999).

Additional evidence linking the solar-minimum streamer belt with the slow solar wind was published by Sheeley et al. (1997). Sheeley et al. studied inhomogeneities in the solar wind from LASCO data of 1996. These inhomogeneities originated at the apex of coronal streamers, at approximately 3–4 $R_{\odot}$, and travel outward as if a portion of the streamer was being torn away. By tracking these dense structures, they determined that they were passively carried by the slow solar wind. In an earlier paper Feldman et al. (1981) identified quiescent near-equatorial coronal streamers as a source of the slow solar wind. This conclusion was based on Vela heavy ion data measured between 1971 and 1977 at 1 AU.

5.2. *FIP Effect*

The FIP effect is a phenomenon seen in the corona and the solar wind where the elements whose first ionization potential is less than 10 eV are more abundant relative to those with a FIP greater than 10 eV. This phenomenon can be studied by using the high-FIP element oxygen, as done here, to determine the FIP bias. The low-FIP elements are typically enhanced by approximately a factor of 4 compared to the high-FIP elements in many parts of the corona and the slow solar wind. This does bring up the question of whether it is the low-FIP element that is enhanced or the high-FIP element that is depleted. The examination of the absolute abundances demonstrate the true nature of this phenomenon. All of the elemental abundances quoted here are normalized relative to their photospheric value (Allen 1973). Examining the FIP effect in this manner has been done previously, for example, by P. Wurz & P. Bochsler (2003, in preparation), who compared the abundance of calcium relative to oxygen and hydrogen derived from CELIAS data during the 1996 solar minimum.

TABLE 2
East Limb Absolute Abundance Results

		Abundances			FIP Bias	
DOY Range	Type	$[O/H]/[O/H]_{ph}$	$[Si/H]/[Si/H]_{ph}$	$[Mg/H]/[Mg/H]_{ph}$	$[Si/O]/[Si/O]_{ph}$	$[Mg/O]/[Mg/O]_{ph}$
154–158.....	AR	0.520 ± 0.078	1.545 ± 0.203	2.653 ± 0.365	2.969	5.097
162–169.....	QL1	0.350 ± 0.231	0.620 ± 0.335	1.801 ± 1.027	1.775	5.150
162–169.....	QL2	0.275 ± 0.160	0.433 ± 0.330	1.368 ± 0.620	1.577	4.979
162–169.....	QC	0.107 ± 0.025	0.317 ± 0.087	0.824 ± 0.150	2.969	7.710
177–185.....	AR	0.377 ± 0.079	1.096 ± 0.290	1.861 ± 0.199	2.909	4.938
191–194.....	QL1	0.327 ± 0.058	0.467 ± 0.055	1.144 ± 0.062	1.428	3.495
191–194.....	QL2	0.227 ± 0.043	0.293 ± 0.071	0.889 ± 0.103	1.289	3.909
191–194.....	QC	0.069 ± 0.014	0.184 ± 0.019	0.554 ± 0.034	2.648	7.993

The oxygen absolute abundances provided in Figures 6 and 7 demonstrate a significant depletion relative to their photospheric values. This result remains true regardless of the streamer structure considered. For active-region streamers the depletion is approximately a factor of 2, while for the quiescent streamer cores the depletion can be over a factor of 10. The quiescent leg structures appear to have an abundance that can fall between the core and the active-region categories. The higher uncertainty of the quiescent leg structures, caused by their lower Lyβ counts compared to the other structures, makes any definitive conclusion difficult. These results are summarized by the streamer structure time period averages listed in Tables 1 and 2.

The magnesium abundances in Figures 8 and 9 are dominated by enhancements for the active-region streamers and the quiescent leg structures. The magnesium abundances reached a maximum enhancement of a factor of 4 for active-region streamers. Although the quiescent leg structures on some occasions (e.g., DOYs 161 and 178 in Fig. 8) reached a maximum enhancement of approximately the same order, the increased error caused by the low Lyβ intensities found in these structures could exaggerate these results. Note that the quiescent cores demonstrate a depletion in the photospheric normalized absolute elemental abundances. As will be discussed shortly, this is a feature that would not be seen if the FIP effect was examined in the traditional manner. The phenomenon responsible for the abundance depletion found in the core structures affects all three elements studied here, regardless of their FIP values.

The abundance results for silicon (Figs. 10 and 11) occasionally indicate enhancements at the peaks of the active-region and quiescent leg structures. However, the overall results from the data indicate abundance values lower than expected for a low-FIP element. This result could reflect the uncertainty in both the UVCS radiometric second-order calibration and the CHIANTI emissivity for the Si XII 499 Å line. Laming & Feldman (1999) indicate a possible problem with the atomic rates of Li-like ions such as Si XII. In addition, Si XII is more sensitive to the electron temperature in the range of $10^{6.0}$–$10^{6.2}$ than O VI and Mg X. The uncertainty in the assumed electron temperature could therefore contribute to this abundance discrepancy. Regardless of the abundance values, the pattern in the results matches those found for oxygen and magnesium. The active-region and quiescent-leg abundances are significantly higher compared to the quiescent core, which is most likely depleted to some degree.

The most significant result from this component of the analysis comes from the comparison of these results with the traditional FIP bias, tabulated in the last two columns of Tables 1 and 2. The FIP bias indicates an enhancement for both silicon and magnesium in active-region streamers and quiescent leg structures. This result agrees with that derived from examining the absolute abundances of these two elements. However, the FIP bias indicates a significant enhancement for silicon and magnesium in quiescent cores. This result is contradictory to what is concluded from the absolute abundances, which is a depletion in the core structures. The reason for this discrepancy lies in the oxygen abundances found in quiescent cores, which are depleted to a much higher degree than magnesium and silicon. This result can bring an erroneous conclusion that these two low-FIP elements are enhanced instead of depleted within the quiescent-core structures. As stated, the concern when analyzing the FIP bias results is whether they indicated an enhancement of the low-FIP elements or a depletion of the high-FIP element. It turns out that for this particular case *both* low- and high-FIP elements are depleted, with oxygen being depleted to a greater degree than magnesium and silicon. Based on these results, the conclusion is that to properly explore this phenomena, the absolute elemental abundances need to be examined.

5.3. *Solar Rotation*

The manifestation of solar rotation can easily be seen in the abundance data, especially for the active-region entries. For instance, the first peak at the west limb (DOY 168 in Fig. 6) and the second peak at the east limb (DOY 182 in Fig. 7) for the oxygen abundances are separated by 14 days, or approximately half a solar rotation. However, this is not always true since even during solar minimum the morphology of a streamer can change notably over the course of 2 weeks. The abundance graphs display the dynamic nature of this "quiet" streamer belt with respect to time and element.

Now the trend in the abundances found for active-region streamers as they approach and recede from the limb are examined. The values of the abundances rise and fall with solar rotation (i.e., time and longitude), reaching a maximum when the active-region streamer longitudinal axis is located near the limb. A significant change in the abundance was observed even over the course of 24 hr. Since this property was found consistently in all six figures, it is most likely an actual physical property. There are two possible explanations for this phenomenon, both of which probably influence the observed abundances. The first is the result of the alignment of the UVCS FOV and the streamer. The UVCS FOV samples the streamer along the line of sight. Unless the longitudinal axis of the streamer is located at the limb the observation will sample heights within the streamer other than or in addition to the one intended. If this is true, it would indicate the abundances are not constant with heliocentric height. The second cause has to do with the three-dimensional structure of the streamer belt and the two types of streamers of which it is composed. The line of sight of the UVCS FOV may pass through several different streamers near the limb. These changes in the projection effects can result in different abundance results. This could be partly responsible for the rapid variance in the abundance values illustrated in Figures 6–11.

There were several occasions when a well-defined quiescent streamer signal was identified within a set of active-region observations (DOY 196 in Figs. 6, 8, and 11). In most of these cases, the abundance calculations confirm a core-type structure although with higher abundances than those found in the quiescent-core data sets. This could be caused by a particularly strong quiescent-streamer structure located somewhere along the UVCS FOV. A second possibility is that a chance orientation of a streamer or a multiple-streamer configuration could mimic the quiescent-streamer signature. A time-dependent three-dimensional model would have to be constructed in order to fully explore the different phenomena described in this section.

5.4. *Comparison with Other Streamer Abundances*

The streamer abundances derived by Ko et al. (2002) and Raymond et al. (1997) are provided in Table 3. To simplify

TABLE 3
Comparison of Absolute Abundances

Element	Ko (2002) Active Region	Raymond (1997)		
		Active Region[a]	Quiescent Leg[b]	Quiescent Core[b]
O.....	0.295[c]	0.479	0.380	0.095
Si	1.259[c]	0.955	0.380	0.151
Mg.....	1.514[d]	1.905	0.955	0.479

[a] 1996 July 23 and 24: 1.7 $R_\odot$.
[b] 1996 July 25: 1.5 $R_\odot$.
[c] 1998 April 7: 1.6 $R_\odot$.
[d] 1998 April 7: 1.48 $R_\odot$.

the comparison their results have been converted from the original dex format to photospheric normalized absolute abundances, using the photospheric values of Allen (1973). The streamer observations of Ko et al. (2002) were conducted on 1998 April 6–7 for an active-region streamer at an angle 120° counterclockwise from solar north. The height for the oxygen and silicon abundances was 1.6 $R_\odot$, while the magnesium abundance was derived at 1.48 $R_\odot$. The Raymond et al. (1997) data come from two separate streamers observed on 1996 July 23 and 24 at 1.7 $R_\odot$ for the active-region streamer on the east limb and on 1996 July 25 at 1.5 $R_\odot$ for the quiescent streamer on the west limb. The observations of Raymond et al. (1997) occurred within the time frame of the data sets reported here.

When the abundances of Table 3 are compared to those found in Tables 1 and 2 for the corresponding structures, a good agreement is found. The values of Table 3 all fall within the range of abundance values indicated by Tables 1 and 2. Additional streamer observations under varied conditions are required before any further interpretation can be achieved. It should also be noted that the rotation effects between the streamer and the UVCS FOV, discussed in the previous subsection, are not considered in the results of Table 3.

6. COMPARISON WITH CELIAS IN SITU RESULTS

Among the in situ experiments aboard *SOHO* is the CELIAS experiment, which is described in Hovestadt et al. (1995). CELIAS can measure the mass, ionic charge, and energy of solar wind ions. From this information the elemental and isotopic abundances can be derived. A sample of the CELIAS data from the time period in question is provided as Figure 12. The magnesium and silicon abundance results are not provided in Figure 12, and the oxygen abundances have not been normalized by their photospheric value.

Daily values of the oxygen, magnesium, and silicon abundances measured by the CELIAS MTOF sensor are illustrated by the shaded regions of Figures 6–11. In order to align the in situ and remote sensor results, the CELIAS abundances were shifted by positive 3 days for the west limb UVCS figures and minus 11 days for the east limb. These adjustments are approximations based on a slow solar wind velocity of 400 km s^{-1}.

The solar wind velocity measured by CELIAS, provided as the lower graph of Figure 12, indicates values typically under 450 km s^{-1}. This means that the slow solar wind was observed by CELIAS for the majority of the observation period. The CELIAS abundances for oxygen and magnesium both possess the same order of magnitude as the UVCS derived values at 1.7 $R_\odot$. The silicon results from CELIAS typically indicate a factor of 2 higher abundance than the UVCS-derived values. As mentioned earlier, this could be the result of the uncertainty of both the UVCS radiometric second order calibration and the CHIANTI emissivity. The CELIAS abundances also exhibit the same highly variable nature as the UVCS results.

This line of evidence supports the concept that the solar-minimum streamer belt is a contributor to the slow solar wind composition as identified by Wang et al. (2000). This is also consistent with the results of Strachan et al. (2002) and Raymond et al. (1997), who both deduced that the quiescent streamer legs were a source of the slow solar wind. Wang et al. (2000) also point out that there are other potential sources of the slow solar wind than small low-latitude coronal holes. It is possible that CELIAS is sampling some combination of slow solar wind sources during this observation period.

7. CONCLUSIONS

1. Streamers have two distinct classes: quiescent streamers, which form above filaments or quiet-Sun regions, are stable structures possessing a highly depleted core; active-region streamers are structures whose dynamic nature makes the formation of a depleted core unlikely.

2. The cores of quiescent streamers containe trapped plasma that probably descends in heliocentric height owing to gravitational settling and results in an abundance depletion of both high- and low-FIP elements. The material contained by the outer magnetic field lines of the streamer is released during the reconnection of these closed field lines with adjoining open magnetic field lines (Schwadron et al. 1999).

3. Evidence of the FIP effect was definitely present in the UVCS data for both active and quiescent streamers at 1.7 $R_\odot$. The absolute abundances showed enhancements in the magnesium (low FIP) and depletion in the oxygen (high FIP) abundances, whereas the silicon results are more problematic and require future investigation. The silicon results indicate depleted abundances, although not as depleted as the oxygen abundances. By examining the absolute elemental abundance ($[X_i/H]/[X_i/H]_{ph}$) in comparison to the traditional FIP bias (e.g., $[X_i/O]/[X_i/O]_{ph}$), a serious complication with the latter is revealed. For quiescent core structures the abundance of oxygen was found to have a higher degree of depletion than magnesium or silicon. As a

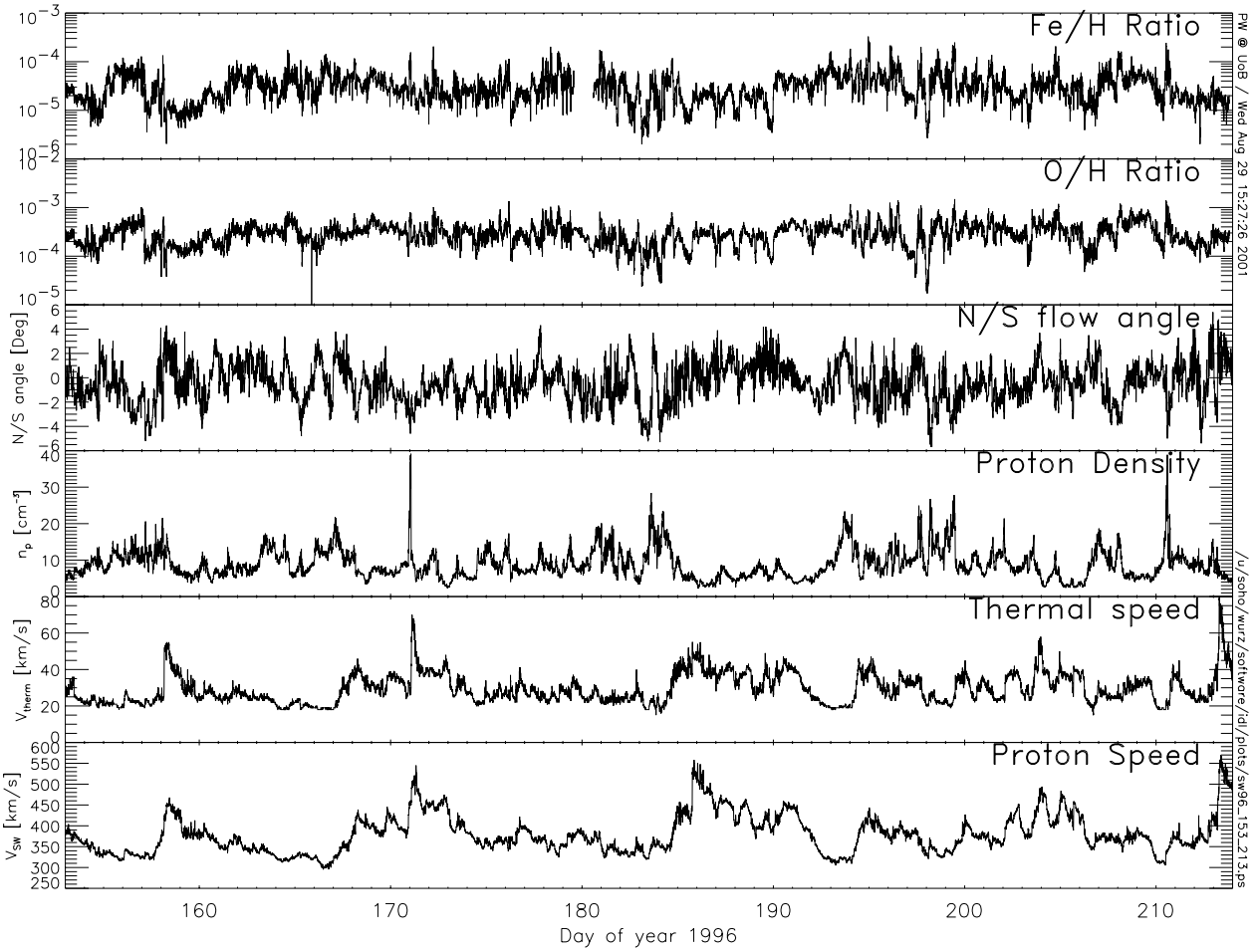

FIG. 12.—Solar wind properties measured in situ by CELIAS PM and CTOF from 1996 June 1 to August 5

result, the FIP bias would indicate an enhancement instead of a depletion as determined by examining the absolute elemental abundances. Therefore, to fully explore the FIP effect phenomena, it would be preferable to utilize the absolute elemental abundances.

4. The abundance values were found to be dependent on the position of the streamer's longitudinal axis relative to the limb. When this axis was located near the limb, the core abundances reached their lowest values while the active-region streamers reached their maximum abundance values. This variance is probably caused by the line of sight sampling multiple heights of an individual streamer and observing several individual streamers. To remove the uncertainty caused by solar rotation effects, the longitudinal streamer axis must be located near the limb, or else a three-dimensional model of the streamer(s) is required.

5. The abundances of Ko et al. (2002) and Raymond et al. (1997) all fall within the range of values presented here.

6. The CELIAS instrument recorded solar wind velocities consistent with the slow solar wind, i.e., below 450 km s^{-1}. The in situ abundance values of oxygen and magnesium agree very well with the remote derived values at 1.7 $R_{\odot}$. The silicon results could possibly be in agreement once the statistical, experimental, and atomic rate uncertainties are removed. Both UVCS and CELIAS observations also displayed the highly variable abundance values seen before in other slow solar wind observations. The conclusion is that the solar-minimum streamer belt is a source of the slow solar wind that probably originates from the outer streamer boundaries.

SOHO is a project of international collaboration between ESA and NASA. This work was performed under NASA grant NAG 5-11420 to the Smithsonian Astrophysical Observatory. P. Wurz is supported by the Swiss National Science Foundation.

REFERENCES

Allen, C. W. 1973, Astrophysical Quantities (London: Athlone)
Delaboudinière, J. P., et al. 1995, Sol. Phys., 162, 291
Dere, K. P., Landi, E., Mason, H. E., Fossi, B. C., Young, P. R. 1997, A&AS, 125, 149
Dere, K. P., Landi, E., Young, P. R., & Del Zanna, G. 2001, ApJS, 134, 331
Feldman, W. C., Asbridge, J. R., Bame, S. J., Fenimore, E. E., & Gosling, J. T. 1981, J. Geophys. Res., 86, 5408
Fisk, L., & Schwandon, N. A. 2001, Space Sci. Rev., 97, 21
Gardner, L. D., Atkins, N., Fineschi, S., Smith, P. L., Kohl, J. L., Maccari, L., & Romoli, M. 2000, Proc. SPIE, 4139, 362
Gardner, L. D., et al. 1996, Proc. SPIE, 2831, 2
———. 2003, in the Radiometric Calibration of *SOHO*, ed. A. Pauluhn, M. Huber, & R. von Steiger (Dordrecht: Kluwer), in press
Habbal, S. R., Woo, R., Fineschi, S., O'Neal, R., Kohl, J., Noci, G., & Korendyke, C. 1997, ApJ, 489, L103
Hovestadt, D., et al. 1995, Sol. Phys., 162, 441
Ko, Y.-K., Raymond, J. C., Li, J., Ciaravella, A., Michels, J., Fineschi, S., & Wu, R. 2002, ApJ, 578, 979
Kohl, J. L., et al. 1995, Sol. Phys., 162, 313
Laming, J., & Feldman, U. 1999, ApJ, 527, 461

Linker, J. A., & Mikić, Z. 1995, ApJ, 438, L45
Marocchi, D., Antonucci, E., & Giordano, S. 2001, Ann. Geophys., 19, 135
Noci, G., et al. 1997, in Fifth *SOHO* Workshop, ed. A. Wilson (ESA SP-404; Norway: ESA), 75
Ofman, L. 2000, Geophys. Res. Lett., 27, 2885
Parenti, S., Bromage, B. J. I., Poletto, G., Noci, G., Raymond, J. C., & Bromage, G. E. 2000, A&A, 363, 800
Pernechele, C., Naletto, G., Nicolosi, P., Poletto, L., & Tondello, G. 1995, Proc. SPIE, 2517, 79
Raymond, J. C., Suleiman, R., Kohl, J. L., & Noci, G. 1998, Space Sci. Rev., 85, 283
Raymond, J. C., et al. 1997, Sol. Phys., 175, 645
Schwadron, N. A., Fisk, L. A., & Zurbuchen, T. H. 1999, ApJ, 521, 859
Sheeley, N. R., et al. 1997, ApJ, 484, 472
Strachan, L., Suleiman, R., Panasyuk, A. V., Biesecker, D. A., & Kohl, J. L. 2002, ApJ, 571, 1008
Suess, S. T., Wang, A.-H., Wu, S. T., & Nerney, S. F. 1999, in Coronal Holes and Solar Wind Acceleration, ed. J. L. Kohl & S. R. Cranmer (Dordrecht: Kluwer), 323
Vásquez, A. M. 2002, Ph.D. thesis, Univ. Buenos Aires
Wang, Y.-M., & Sheeley, N. R. 1991, ApJ, 372, L45
Wang, Y.-M., Sheeley, N. R., Socker, D. G., Howard, R. A., & Rich, N. B. 2000, J. Geophys. Res., 105, 25, 133
Wang, Y.-M., et al. 1997, ApJ, 485, 875
———. 1998, ApJ, 498, L165
Woo, R., & Martin, J. 1997, Geophys. Res Lett., 24, 2535